

Chapter 5

Bandlimited raypaths

This final chapter links infinite bandwidth ray-trace tomography and monochromatic wave-equation tomography with the introduction of bandlimited raypaths. The chapter is divided into two sections. The first defines bandlimited raypaths; the second provides an example comparing ray and bandlimited ray inversion.

5.1 Theory

The preceding four chapters have shown that wave-equation tomography is superior to ray-trace tomography both in dealing with geometrical frequency dispersion and in inverting finite aperture data. The method achieves this superiority because it is monochromatic, representing one extreme of the uncertainty relation:

$$\Delta t \Delta \omega \geq 1/2. \tag{5.1}$$

Since $\Delta \omega$ is infinitely small, Δt is infinitely long and the entire seismic coda is utilized in the inversion. The method accounts for scattered energy arriving at any time from any distance and its wavepath backprojection patterns cover the entire x, z plane. Unfortunately, wave-equation tomography's superiority is gained at the expense of robustness. Because it is monochromatic, modeled events cannot be windowed from unmodeled events in time: all of the signal and noise on a trace must be dealt with simultaneously.

Ray-trace tomography is more robust than wave-equation tomography because it selects as signal the time delay of one well understood event. Instead of inverting amplitude

changes and phase delays for single frequencies, it inverts the slope of a phase-delay vs. frequency curve that is assumed to be linear over an infinite bandwidth. The method represents the other extreme of the uncertainty principle, where Δt is infinitely short and $\Delta\omega$ infinitely large.

In real seismic applications phase delay is rarely linear and bandwidth is never infinite. The uncertainty inherent in picking a peak from a distorted, bandlimited wavelet is usually incorporated in ray-trace tomography only indirectly. Algorithms generally acknowledge that raypaths are far higher in wavenumber than the model being inverted by smoothing the inversion in one of four ways. First, the final cell representation can be bandpassed. Second, the model can be parameterized in terms of smooth basis functions instead of cells, reducing the high-wavenumber indeterminacy and expense of the problem at the outset (Dziewonski et al., 1977; Van Trier, 1988). Third, the indeterminacy can be removed by imposing smoothness constraints on the model during the inversion with damped least squares (Menke, 1984a; Sword, 1988). Fourth, the result can be smoothed by broadening the backprojection raypaths themselves with convolutional quelling (a specialized form of weighted, damped least squares; Meyerholtz et al., 1989).

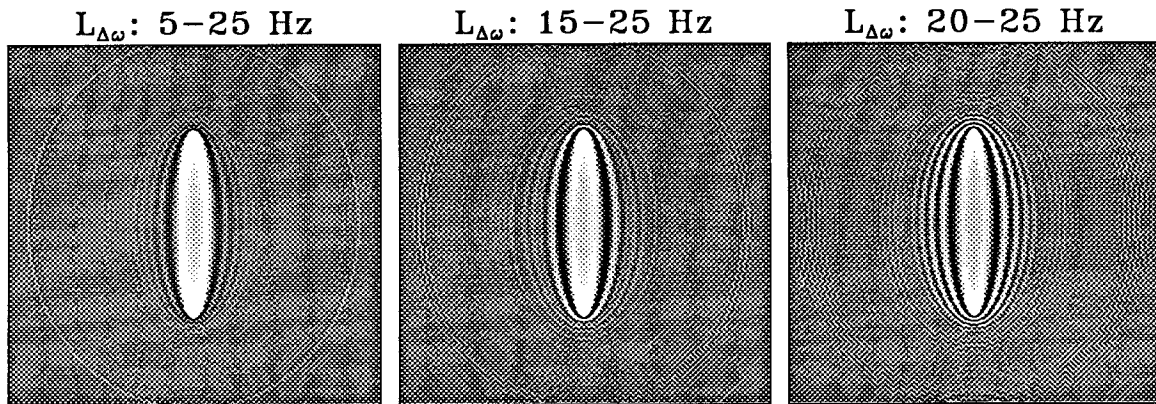
Transmission-geometry Rytov wavepaths provide a way of incorporating bandwidth and uncertainty information into ray-trace tomography in a more direct and physically reasonable fashion. Ray tomography can be redefined as Rytov tomography under a nondispersive constraint: with $\Im(\Delta\Phi)$ and $\Re(\Delta\Phi)$ assumed to be linear in frequency and zero, respectively, over a specified bandwidth. Under this definition the traveltime delay picked for an event becomes a normalized average of imaginary phase perturbations over frequency:

$$\Delta t = \frac{1}{\Delta\omega} \int_{\omega_{min}}^{\omega_{max}} \frac{\Im[\Delta\Phi(\omega)]}{\omega} d\omega. \quad (5.2)$$

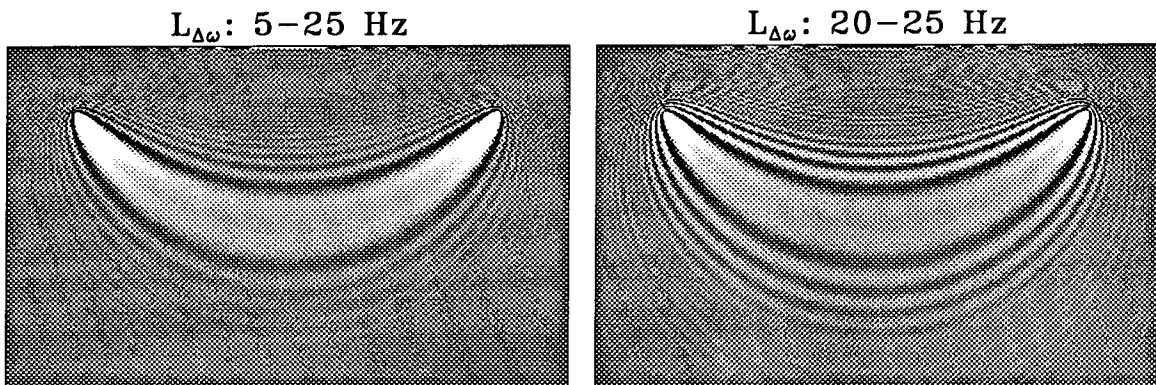
The appropriate backprojection pattern becomes a similar normalized average of imaginary wavepaths over frequency:

$$L_{\Delta\omega}(\mathbf{r}) = \frac{1}{\Delta\omega} \int_{\omega_{min}}^{\omega_{max}} \frac{\Im[\mathcal{L}_0(\omega, \mathbf{r})]}{\omega} d\omega. \quad (5.3)$$

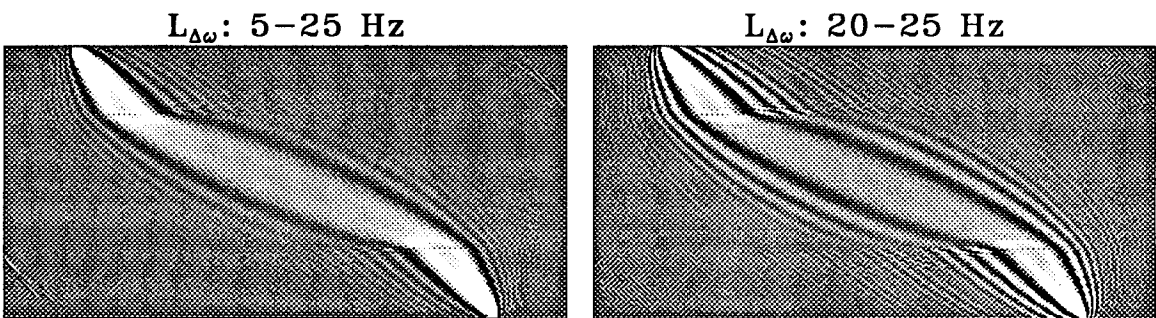
Figure 5.1 shows examples of such *bandlimited raypaths* $L_{\Delta\omega}$ formed by numerically integrating imaginary, monochromatic, Rytov wavepaths from 5 to 25 Hz, 15 to 25 Hz, and



a) Constant velocity background



b) Velocity gradient background



c) Layered velocity background

FIG. 5.1. 2-d bandlimited raypaths $L_{\Delta\omega}$. (a) Constant velocity background field. (b) Velocity gradient background field. (c) Layered velocity background field.

20 to 25 Hz. Rows (a) through (c) correspond to the two-dimensional Rytov wavepaths pictured in Figures 3.1, 3.3 and 3.4: for constant, vertical gradient and layered background velocity models, respectively. Clearly, the rapidly oscillating outer regions of the wavepaths have cancelled while the smooth, first-Fresnel zones have added. Three observations can be made about these bandlimited raypaths—the wave-theoretic equivalents of Hagedoorn’s beams.

First, they graphically illustrate how the extra information in full waveform inversion is lost when an event is specified by a single time pick. Windowing an event in the time domain smooths the event in the frequency domain: only when the medium is nondispersive is the discarded high-wavenumber information redundant.

Second, because they take scattering into account, the bandlimited raypaths are high in amplitude at the source and receiver and low in amplitude elsewhere. This weighting is an expression of wavefront healing (Clærbout, 1985). In contrast to traditional ray-trace tomography, a velocity perturbation close to the source or receiver will have a much larger impact on the recorded signal than a more distant perturbation of similar magnitude.

Third, and most importantly, the breadth of the bandlimited raypaths depends inversely on the width of the frequency band summed over and not on the central frequency of the band. Imaginary Rytov wavepaths can be defined as *monochromatic raypaths*;¹ bandlimited raypaths can be imagined as collapsing to traditionally narrow raypath patterns for infinite bandwidth. The inverse relation between width and bandwidth is shown in more detail in Figure 5.2, with plots of half cross sections through 3-d bandlimited raypaths for different combinations of ω_{min} and ω_{max} . While the relation is demonstrated more mathematically in Appendix B, it can be derived most intuitively from the uncertainty relation. In the uncertainty relation Δt corresponds to the time window of the trace examined (i.e., for traveltimes, the sample rate). Since it dictates the averaging of frequency information in the Fourier domain, it is inversely proportional to the bandwidth of the applicable bandlimited raypath. Because it also limits the distance detectable scatterers can stray from the Fermat path, it is directly proportional to the bandlimited

¹In his interesting comparison of rays and waves, Foreman (1989) also points out that ray theory is essentially broadband, as evidenced by the multipathing characteristic of ray tracing. He defines single-path, frequency-dependent *exact rays* as solutions to $dx/d\sigma = \Im(\nabla\psi(\omega)/\psi(\omega))$. Uniquely determined by takeoff angle, exact rays could serve as an alternative to imaginary Rytov wavepaths in my definition of monochromatic raypaths. However, because they follow what is a null zone in an imaginary three-dimensional Rytov wavepath, they offer little information about a frequency’s sensitivity to velocity perturbations—and consequently little application in tomographic inversion.

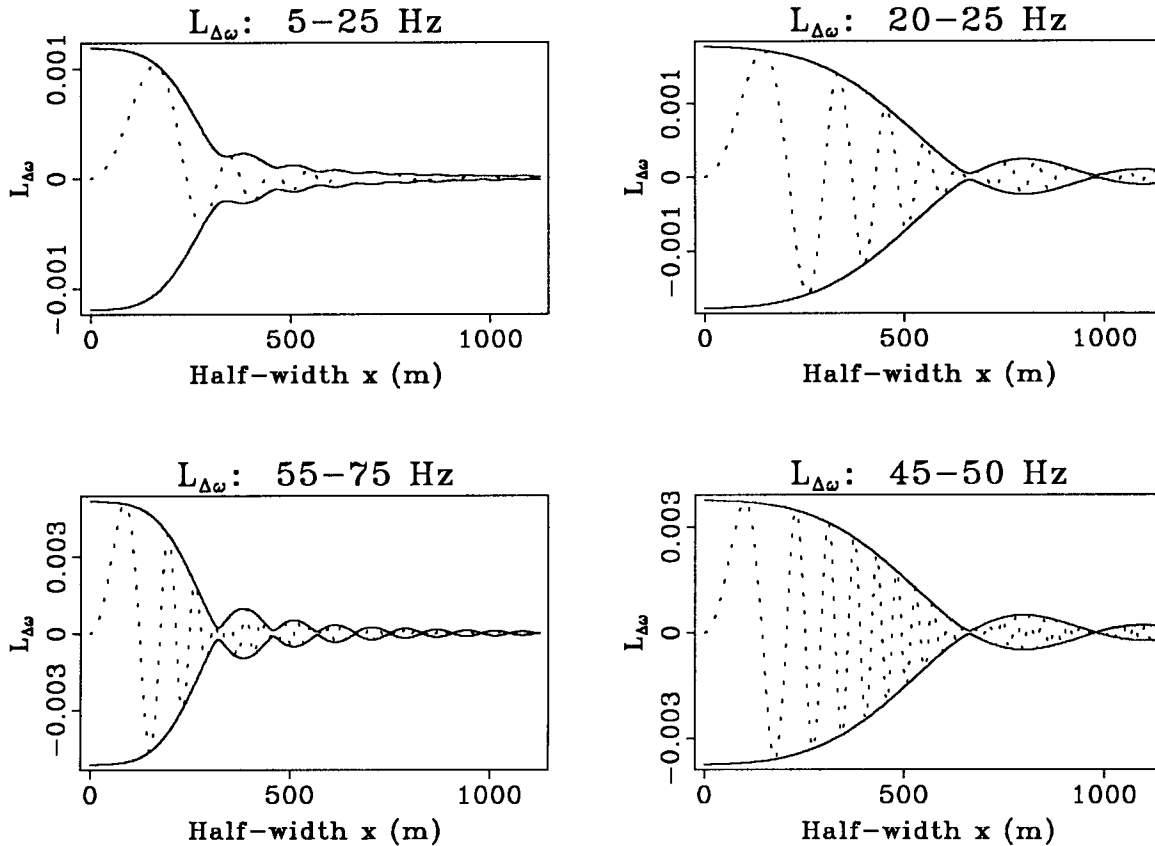


FIG. 5.2. Bandlimited-raypath width. Half cross sections through 3-d constant-velocity bandlimited raypaths (dotted lines) and their envelopes (solid lines) for four different combinations of ω_{min} and ω_{max} . The cross section is taken midway between the source and receiver; the source-receiver separation is 2000 m; and the background velocity is 2000 m/s.

raypath's width.

The bandlimited raypath equivalent of the reflection-geometry wavepath in Figure 3.5 was deliberately omitted from Figure 5.1. Since a linear relation between phase delay and frequency does not hold for this case, a bandlimited transmission raypath cannot be defined.

5.2 Example

The data used for this example were provided by ARCO Oil and Gas Company. They were drawn from a 9-component VSP data set, with four surface-source locations (roughly in line) and a single receiver moved up and down a 1250-meter well. Only first-arrival p-wave events were considered, as recorded on the vertical-source vertical-receiver component.

268 VSP traces

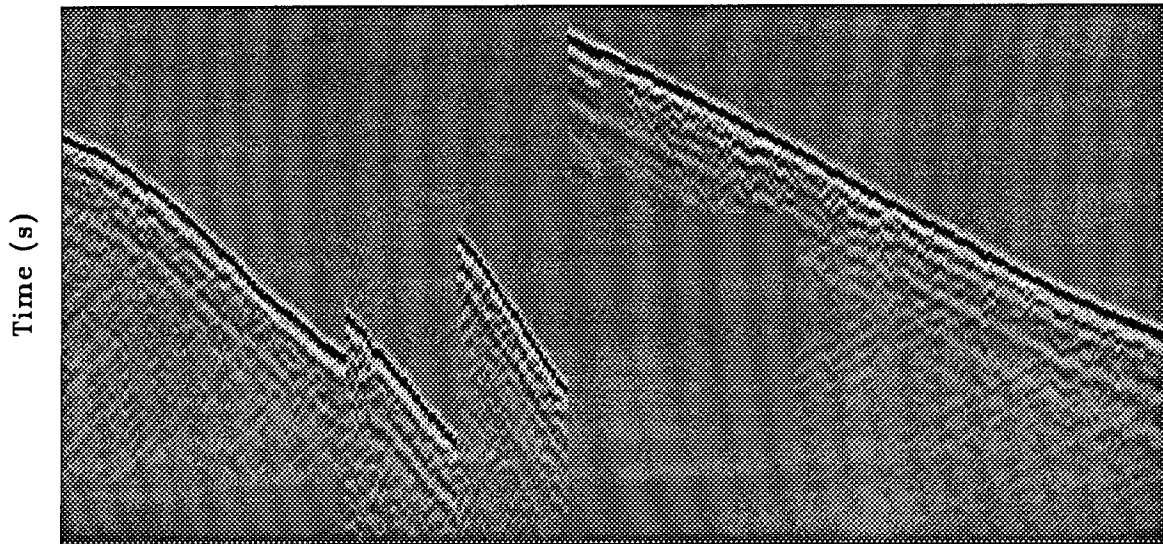


FIG. 5.3. 268 VSP traces.

Figure 5.3 shows the 268 source-receiver traces of the experiment, crudely windowed after the p-arrival and trace balanced for display. From left to right the traces show the 69, 27, 27 and 145 receivers corresponding to the second, third, fourth and first sources from the well. The relative locations of the sources are described below. Figure 5.4 shows the average amplitude-spectrum of the experiment.

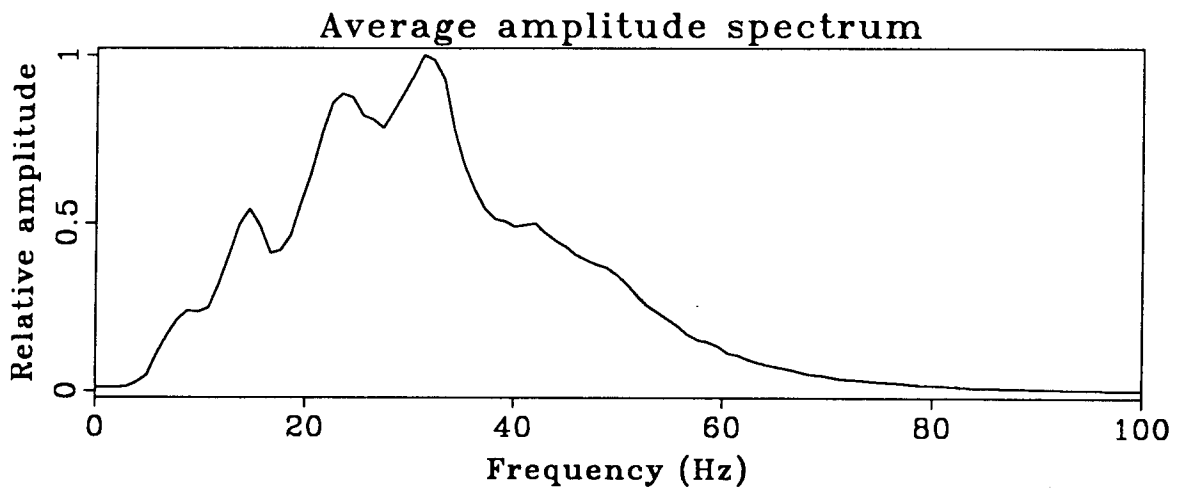


FIG. 5.4. Average amplitude spectrum.

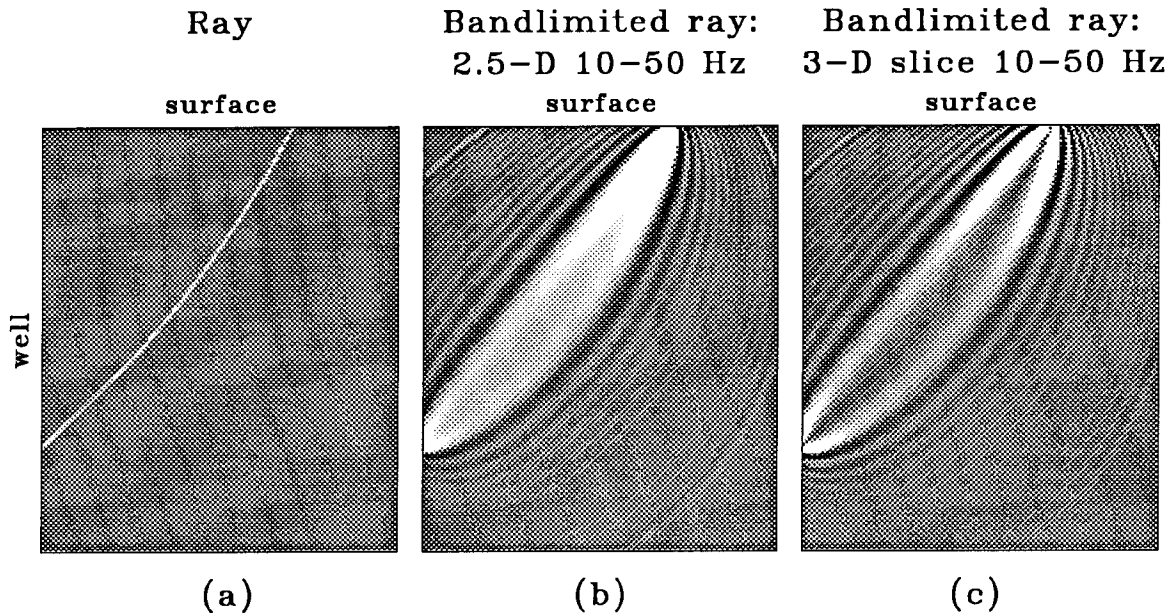


FIG. 5.5. Backprojection patterns. (a) Raypath. (b) 2.5-d bandlimited raypath, $\Delta\omega = 10 - 50$ Hz. (c) Slice through a 3-d bandlimited raypath, $\Delta\omega = 10 - 50$ Hz.

5.2.1 Backprojection patterns

Because the geology in the area was known to be flat, the background velocity model was chosen to increase linearly with depth: $v(z) = 1450 + 1.05z$ in m/s. Regular and bandlimited raypaths through the background model are shown for one shot-geophone pair in panels (a) and (b) of Figure 5.5. The bandlimited raypath is 2.5-dimensional. It was formed by numerically integrating 3-dimensional monochromatic Rytov wavepaths from 10 to 50 Hz and then by numerically integrating these patterns over the out-of-the-page dimension. Panel (c) shows a slice through the full, 3-dimensional bandlimited raypath for comparison. In all cases, the free surface was ignored. Also, while the patterns are cut off at the well in the figure, the full patterns were used in the inversion. Panels (a) and (b) in Figure 5.6 show the composite coverage of regular and bandlimited raypaths for the full data set.

5.2.2 Inversions

The bottom two panels in Figure 5.6 compare the ray and bandlimited-ray velocity inversions achieved after one linear step (implemented as in chapter 4 with LSQR). The results are plotted as perturbations to the background velocity field, $v_1 - v_0$. For the ray inversion, first-break traveltimes were projected back over raypaths; for the

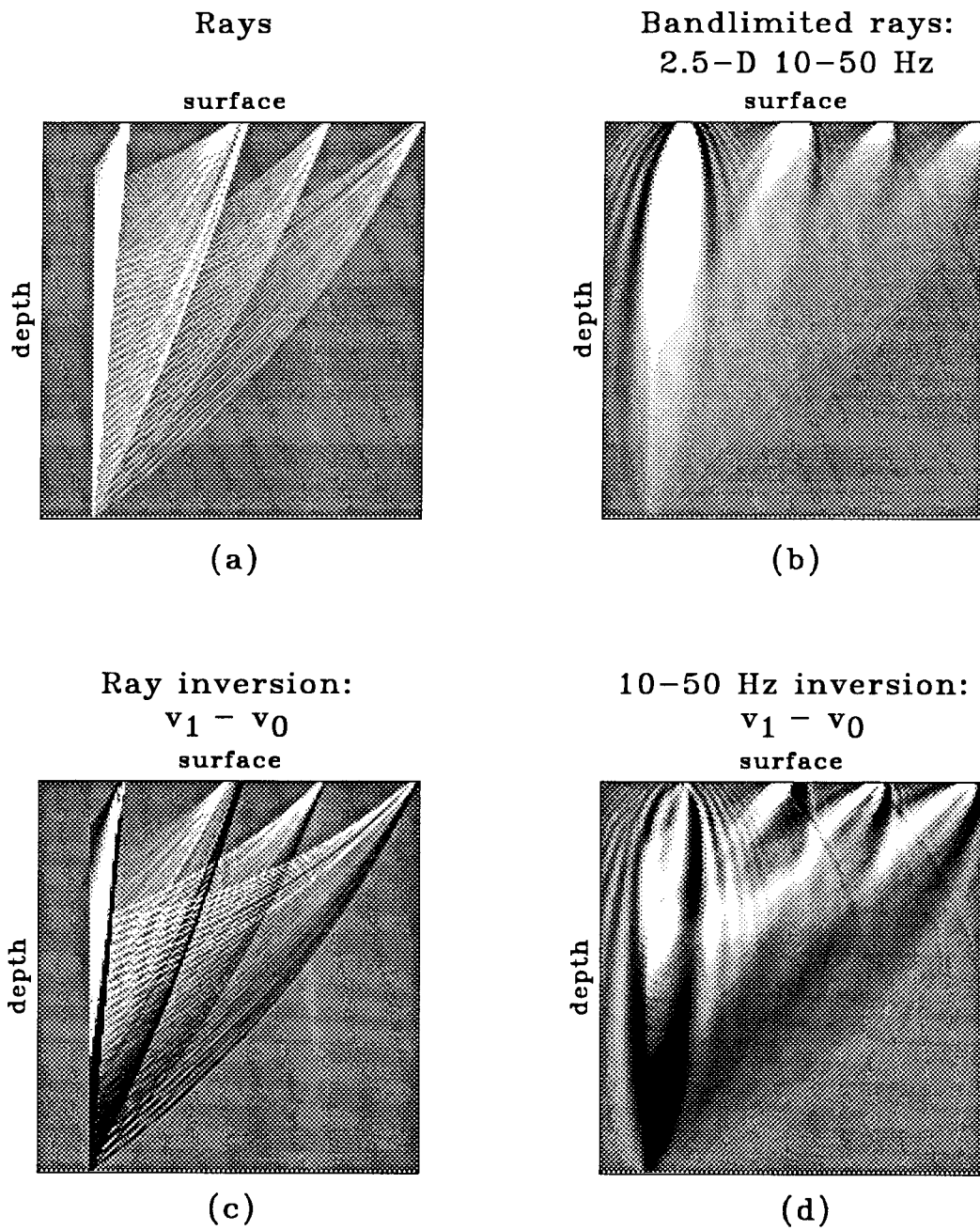


FIG. 5.6. (a), (b) Composite coverage of regular and 10-50 Hz bandlimited raypaths. (c), (d) Ray and 10-50 Hz bandlimited-ray inversions.

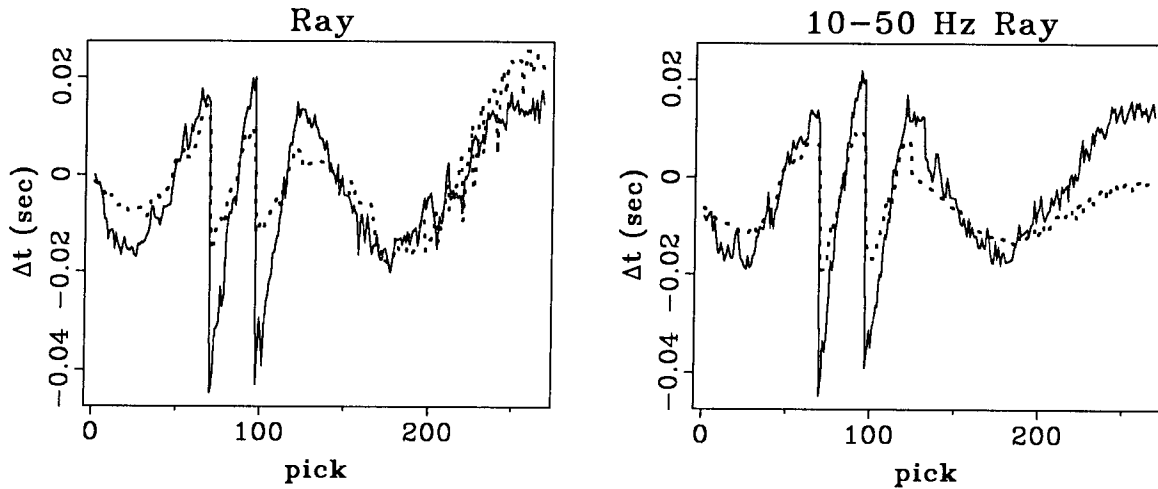
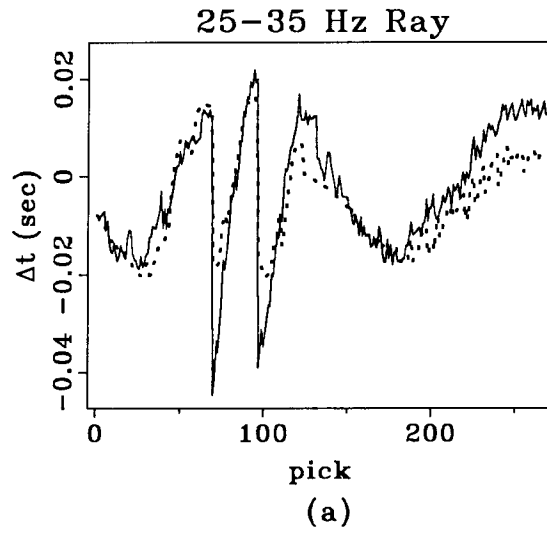


FIG. 5.7. Observed versus predicted data for the ray and 10-50 Hz bandlimited-ray inversions. Solid curves: observed traveltime delays Δt . Dotted curves: traveltime delays predicted by forward modeling through the inversion results ($L_0\Delta w$ and $L_{\Delta\omega}\Delta v/v$).

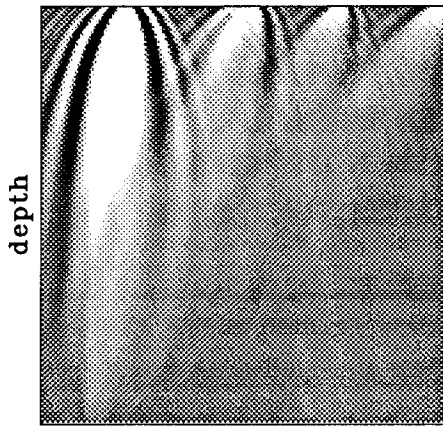
bandlimited-ray inversion, first-peak traveltime delays were projected back over 10-50 Hz bandlimited raypaths. (In recognition of the amplitude spectrum's influence on the first-peak time picks, the wavepaths were amplitude-spectrum weighted before summation in equation 5.3.) Both inversions indicate high relative velocities in the top half of the section and low relative velocities in the bottom half. The bandlimited inversion is noticeably smoother than the ray inversion and it incorporates geometrical-spreading effects. Because the problem was severely underdetermined, the inversions are very similar to the coverage plots in the upper two panels.

The solid curves in the left and right panels of Figure 5.7 show the observed traveltime delays used as data in the ray and bandlimited-ray inversions. The picks along the horizontal axes sequentially plot the source-receiver experiments in the same order as Figure 5.3: from shallowest to deepest for the second, fourth, third and first sources from the well. The dotted curves in Figure 5.7 show the predicted delays calculated by ray and bandlimited-ray forward modeling through the inversion result. The prediction errors (the differences between the observed and predicted traveltime delays) are similar for the ray and bandlimited-ray inversions, except for the closest shot's deepest receivers. Since the broad backprojection patterns for these source-receiver experiments interact almost entirely with the most overdetermined part of the velocity field, their failure to explain the data is not surprising.

Figure 5.8 shows the prediction errors, composite coverage and result for a 25-35 Hz

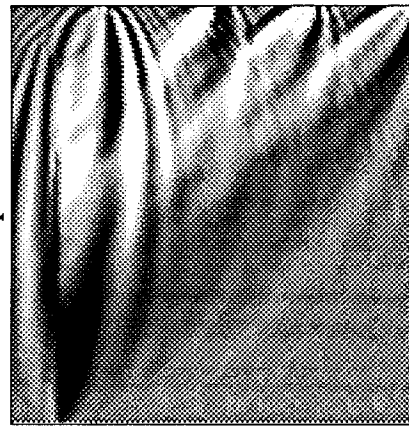


Bandlimited rays:
2.5-D 25-35 Hz
surface



(b)

25-35 Hz inversion:
 $v_1 - v_0$
surface



(c)

FIG. 5.8. 25-35 Hz bandlimited-ray inversion. (a) Prediction errors (25-35 Hz equivalent of Figure 5.7). (b) Composite coverage (25-35 Hz equivalent of Figure 5.6a). (c) Inversion result (25-35 Hz equivalent of Figure 5.6b).

bandlimited-ray inversion. The prediction errors for this implementation are noticeably smaller than for either the ray or 10-50 Hz inversion. Because the source wavelet in the traces of Figure 5.3 is distorted by scattering and geometrical frequency dispersion, the picked data provide a good estimate of the average traveltime delay for the dominant source frequencies and a poor estimate for the subordinate ones. This frequency-dependence emphasizes the determination of seismic-event traveltime picks by frequency content and suggests the simultaneous inversion of separate bandregions.